HIGH POWER LASER
SCIENCE AND ENGINEERING

RESEARCH ARTICLE

A comprehensive diagnostic system of ultra-thin liquid sheet targets

Ziyang Peng [1], Zhengxuan Cao[1,2], Xuan Liu [1], Yinren Shou[3], Jiarui Zhao[1], Shiyou Chen[1], Ying Gao[1], Pengjie Wang[4], Zhusong Mei[1], Zhuo Pan[1], Defeng Kong[1], Shirui Xu[1], Zhipeng Liu[1], Yulan Liang[1], Tianqi Xu[1], Tan Song[1], Xun Chen[1], Qingfan Wu[1], Yujia Zhang[1], Zihao Zhang[1], Xueqin Yan[1,5,6], and Wenjun Ma [1,5,6]

[1] *State Key Laboratory of Nuclear Physics and Technology, School of Physics, Peking University, Beijing, China*

[2] *National Key Laboratory of Shock Wave and Detonation Physics, Institute of Fluid Physics, China Academy of Engineering Physics, Mianyang, China*

[3] *Center for Relativistic Laser Science, Institute for Basic Science, Gwangju, Republic of Korea*

[4] *Institute of Radiation Physics, Helmholtz-Zentrum Dresden Rossendorf, Dresden, Germany*

[5] *Beijing Laser Acceleration Innovation Center, Beijing, China*

[6] *Institute of Guangdong Laser Plasma Technology, Guangzhou, China*

(Received 31 July 2023; revised 4 December 2023; accepted 11 December 2023)

Abstract

To meet the demands of laser-ion acceleration at a high repetition rate, we have developed a comprehensive diagnostic system for real-time and *in situ* monitoring of liquid sheet targets (LSTs). The spatially resolved rapid characterizations of an LST's thickness, flatness, tilt angle and position are fulfilled by different subsystems with high accuracy. With the help of the diagnostic system, we reveal the dependence of thickness distribution on collision parameters and report the 238-nm liquid sheet generated by the collision of two liquid jets. Control methods for the flatness and tilt angle of LSTs have also been provided, which are essential for applications of laser-driven ion acceleration and others.

Keywords: diagnostics; laser-ion acceleration; liquid sheet targets

1. Introduction

The interaction of ultra-intense laser pulses with micrometer-thin film targets can accelerate ions to very high energy within a few micrometers. Near-100-MeV protons and 1.2-GeV Au ions have been generated by laser acceleration[1,2]. This novel ion acceleration method has attracted widespread attention as it can produce ultrashort ion pulses in a short distance, which is highly appealing for applications such as proton imaging, pulsed neutron generation and FLASH radiotherapy[3,4]. Many of them require a high average flux, which should be achieved by shooting targets at a high repetition rate. However, solid films, the most widely used targets in previous studies[5–7], are not suitable for long-term high-repetition-rate shooting. After each laser–target

interaction, the film in an area of about a few mm² around the focal spots would be completely destroyed[8]. If they are shot at kHz, for example, supplying the targets in the vacuum would be a big challenge, not to mention the cost and debris damage to the optical components in the target chamber.

Superior to solid films, free-flowing micrometer-thin liquid sheets are promising targets for high-repetition-rate laser-ion acceleration[9]. They are made of continuous liquid flow without any supporting substrate. Under the irradiation of an ultra-intense laser pulse, the damaged area can be self-repaired in 0.1 ms, enabling continuous shooting at a repetition rate up to the kilohertz or higher level[9]. Therefore, liquid sheet targets (LSTs) have drawn increasing interest in the field of laser-ion acceleration. While still in its early stages, some pioneering works have successfully employed LSTs in experiments. In 2018, Morrison *et al.*[10] first achieved the generation of 2.3 MeV protons from LSTs at a kHz repetition rate for the first time, and a few years later Puyuelo-Valdes *et al.*[11] obtained 3.5-MeV protons

1

from LSTs at a higher vacuum degree. Recent works on cryogenic jets have demonstrated the potential of liquids in generating high-energy ions[12], and deuterons with energies up to 4.4 MeV were also generated by using LSTs made of heavy water[13].

Nevertheless, these works lack a complete characterization of LSTs. It is known that the film's position with respect to the focal spot and its thickness significantly influence the energy of ions. The tilt angle and flatness of the film would affect the direction and divergence of the ion beam. Therefore, for optimized and stable ion acceleration, comprehensive characterization of films is necessary.

In this work, we present an online diagnostic system for the comprehensive characterization of LSTs prepared for laser-ion acceleration. Firstly, an overview of our LST generation and characterization system is presented. Afterwards, the components of the system for measuring an LST's thickness, flatness, tilt angle and spatial position are described separately. Analysis and detailed information about these modules are also provided. Finally, a summary and future prospects are given.

2. Liquid sheet target generation and characterization system

The liquid sheets were generated with our homemade colliding-jet device[14]. Figure 1(a) shows the formation process of a liquid sheet: two liquid jets eject from 50-μm-diameter capillaries and collide at a speed of approximately 20 m/s and a collision angle of 60° (2θ). After the collision, the lateral momenta of the two jets cancel out each other and form a closed liquid sheet in the orthogonal direction due to the effect of surface tension, as shown in Figure 1(b). In this work, we have made improvements to the device to achieve stable control and precise characterization of the liquid sheets. The total degrees of freedom are eight, including 6D

translation and rotation, and relative 2D adjustment between the two jets.

The liquids were driven by two high-performance liquid chromatography (HPLC) pumps (Shimadzu, LC-20ADXR) and injected into two capillaries separately. The capillaries are made of fused silica and the end face of each capillary is polished to decrease the surface roughness around the exit. The back pressure is typically tens of MPa, depending on the length of the capillary, the flow rate and the viscosity of the liquid. The liquids used in this work are mixed solutions of water, glycerol and ethanol. By mixing the three kinds of liquids, the viscosity and surface tension of the solution can be continuously adjusted over a wide range, which we found to be very favorable for the control of the sheets. Glycerol aqueous solutions with a mass fraction between 30% and 70% stably form sheets in our system. This type of liquid is cheap and non-toxic, and has a low saturated vapor pressure, making it ideal for LSTs.

Figure 1(c) shows an overview of the diagnostic system, which allows for real-time and spatially resolved characterization of an LST's thickness, flatness, tilt angle and position, fulfilled by different subsystems. The dashed boxes represent these subsystems, and the purple words next to them describe their functions. These subsystems can be moved by linear stages. All of these subsystems can work online, but the position measurement and tilt angle measurement cannot be performed simultaneously. The confocal detector typically will be moved away after the position measurement. The green light pass in Figure 1(c) represents the probe light for the flatness measurement (multiple co-propagating lasers with different wavelengths), and the yellow light on the right-hand side represents the broadband probe light for the thickness measurement. It should be noted that Figure 1(c) is not drawn to scale. Further details of the subsystems will be presented in the following sections sequentially, and a summary of their features can be found in Section 6.
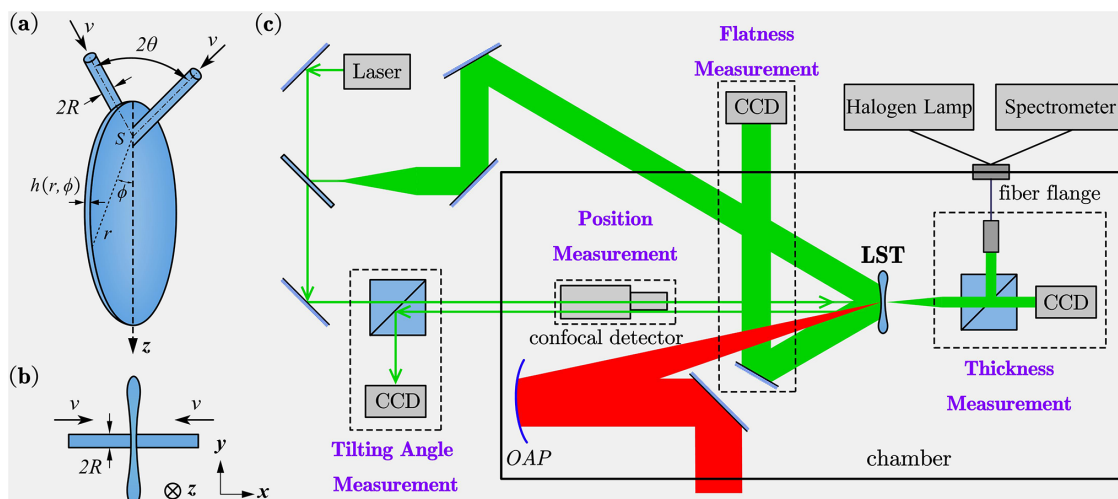

Figure 1. (a) Schematic of liquid sheet generation. (b) Top view of liquid sheet generation. (c) Overview of the main modules of the diagnostic system.

3. Thickness measurement

The target thickness significantly affects the ion energy and the acceleration mechanism[15]. Therefore, it is essential to measure the thickness of the liquid sheet accurately. This could be challenging because LSTs are self-supporting and unable to withstand external force, making contact measurements inapplicable. Besides, the thick edge of the sheet also hinders thickness measurement using side imaging[16]. To address these challenges, we measure the thickness of an LST using the reflected white light spectrum from the film surface. In the following text, we will refer to this method as reflectance spectroscopy.

A schematic diagram of our device can be found in the upper right-hand corner of Figure 1(c). A halogen lamp and a spectrometer are both placed outside the chamber, and two optical fibers are bunched on the feeding flange and connected to the chamber. Figure 2(a) shows a more detailed diagram: the white light emitted from the halogen lamp is focused by the microscope lens and then irradiated on the LST, and the reflected light is sent back to the spectrometer via optical fibers behind the lens. The microscopic objective enables simultaneous imaging of the LST, while white light provides illumination. In order to increase the signal, six optical fibers are used to collect the reflected light. They hexagonally surround the central fiber that connects to the halogen lamp. Figure 2(b) shows the side and front views of the LST, where the bright dot in the center of the sheet is the incident white light. The central fiber serves as the light source, while the six outer fibers gather the reflected light signals, as depicted by the six blue dots in Figure 2(a). The diameter of each fiber is 200 µm, and the spot focused on the sheet is approximately 20 µm. In the next section, it will be seen that the thickness of the liquid sheet is uniform in this small area.

Interference between the two surfaces of the film results in a chirped oscillation in the reflected light spectrum (it displays gradually changing periods, with higher frequency at short wavelengths and lower frequency at long wavelengths). The reflectivity follows Equation (1)[17]:

$$R(h, \lambda, \theta) = \frac{4R_0(\lambda, \theta)\sin^2\left[\delta(h, \lambda, \theta)/2\right]}{\left[1 - R_0(\lambda, \theta)\right]^2 + 4R_0(\lambda, \theta)\sin^2\left[\delta(h, \lambda, \theta)/2\right]},$$
(1)

where $\delta(h, \lambda, \theta) = \frac{4\pi n(\lambda) h \cos\theta'}{\lambda}$ is the phase difference, λ is the wavelength of light, θ is the angle of incidence and θ' is the refraction angle in film, $R_0(\lambda, \theta)$ is the interface reflectivity determined by Fresnel law, h is the thickness of the film and $n(\lambda)$ is the refractive index of the material.

The blue curve in Figure 2(c) shows a typical spectrum measured from an LST, which can be well fitted by assuming a thickness of 1244 nm. However, the fitting method is time-consuming and therefore difficult to use in real-time thickness measurement. Reflectance spectroscopy reported
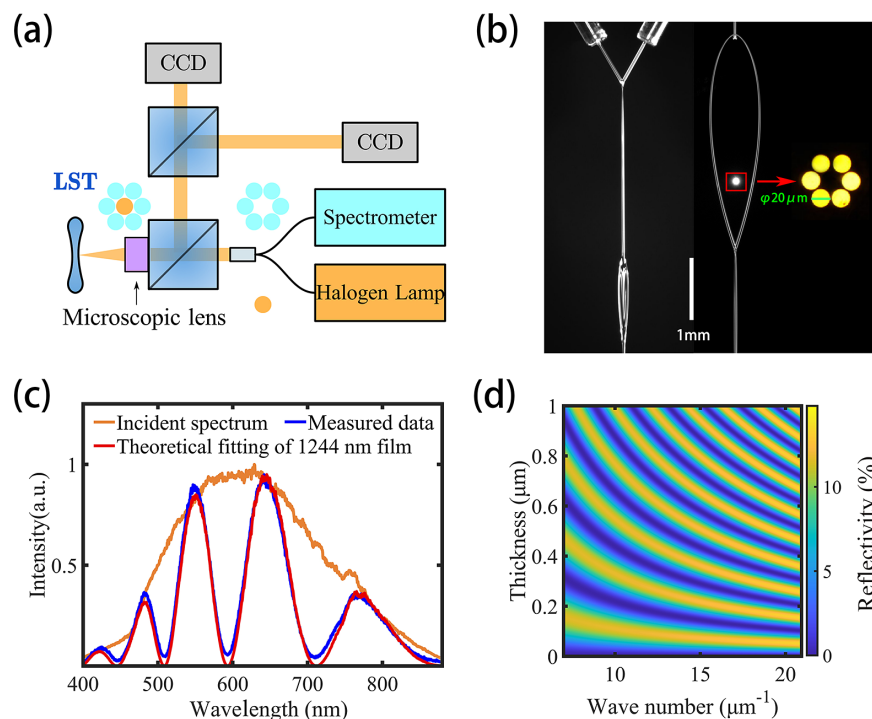

Figure 2. (a) Schematic diagram of reflectance spectroscopy. (b) Side view and front view of the LST; the light source is connected to the six cores here to clearly display the measurement point. (c) A typical reflected spectrum of the LST with the theoretical fitting curve. (d) Theoretical reflectivity of films with different thicknesses at different wave numbers.
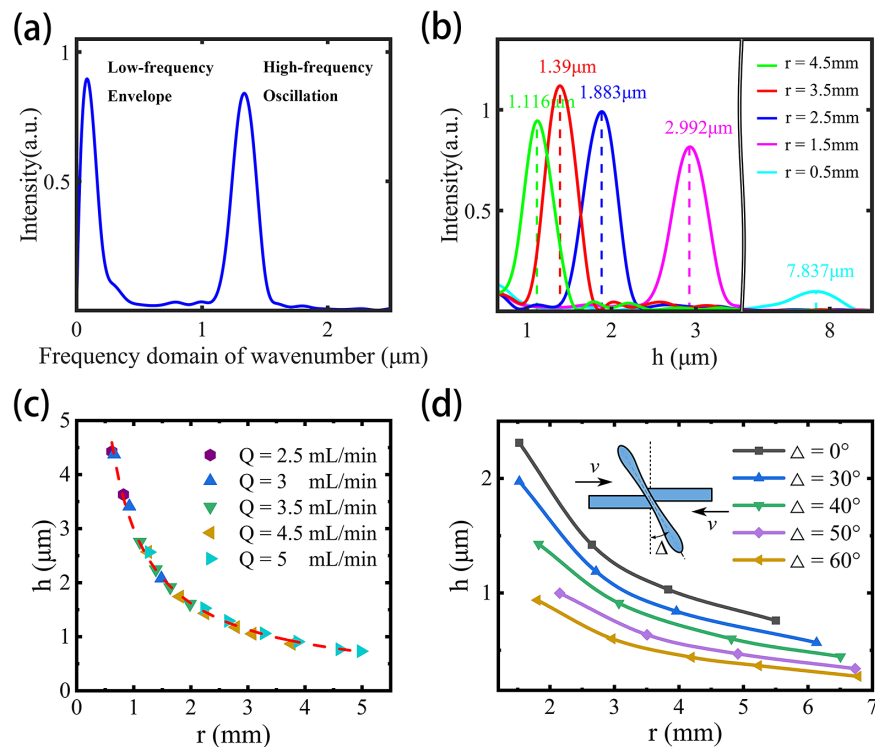
Figure 3. (a) Fourier transform of a measured spectrum in wave number space. (b) Reflected spectrum of an ultra-thin liquid sheet at 238 nm with the theoretical fitting. (c) Thickness of the LST at different flow rates and positions. (d) Thickness of the LST at different misalignments of the colliding jets.

previously mostly used peak positions to calculate the thickness[18], which was highly efficient, but this resulted in low information utilization and lack of accuracy.

Therefore, we develop a fast algorithm to accurately extract thickness information from the reflection spectra, the principle of which is as follows. Figure 2(d) gives theoretical reflectivity values at $\theta = 0°$ as a function of thickness and wave number. It can be seen that for films with thicknesses ranging from hundreds of nanometers to several micrometers, there are multiple peaks in the spectral range of 300–1000 nm for each thickness, and the oscillation interval in the wave number space is constant and proportional to the thickness. This can be derived from Equation (1): the reflectivity exhibits a periodic oscillation, with an instantaneous frequency of $\nu(\lambda, h) = \frac{2n(\lambda)h}{\lambda^2}$. In k-space, the instantaneous frequency is $\nu(k, h) = \frac{n(k)h}{\pi}$, which can be considered a constant if the film is uniform and the dispersion curve is known. By performing Fourier transform on the reflection spectrum, its peak directly corresponds to the thickness.

Figure 3(a) shows an example of the Fourier transform of the measured spectrum in wave number space. There are two peaks in the frequency domain, the low-frequency envelope and the high-frequency oscillation of the spectrum, respectively. The high-frequency peak position is proportional to the thickness, while the low-frequency peak is caused by the slowly changing envelope of the spectrum, as shown in the incident spectrum in Figure 2(c). It should be

clarified that the incident spectrum can only be used as a relative reference. We can normalize the measured spectrum by the incident spectrum to minimize the impact of the low-frequency envelope, but this does not ensure getting absolute reflectivity. The precision of this method is higher than directly measuring the peak positions, as the peak positions are modulated by the spectrum envelope. The inherent low-frequency component sets a lower limit for the measurement, as the oscillation will be masked by the envelope when its frequency is close to the envelope frequency. In our system, the minimum measurable thickness is about 200 nm, which is competent for the current LST (the reported thinnest liquid sheet produced by colliding jets is 450 nm[10]).

Based on this method, we measured the thickness of LSTs at different flow rates along the z-axis. As defined in Figure 1(a), we will use these symbols in the following text: h means the thickness of the LST, r is the distance to the colliding point and ϕ is the azimuth angle of the colliding point. The results of different flow rates and positions are shown in Figure 3(c), all measured points here are $\phi = 0°$ and r takes different values.

As the distance from the collision point increases, the liquid sheet gradually becomes thinner. The thickness at different flow rates appears to fall on the same curve, showing that it is independent of the fluid flow rate. For our application, we always hope to increase the flow rate as much as possible to generate a thinner sheet, but this is limited by factors such as system pressure and fluid instability. A higher
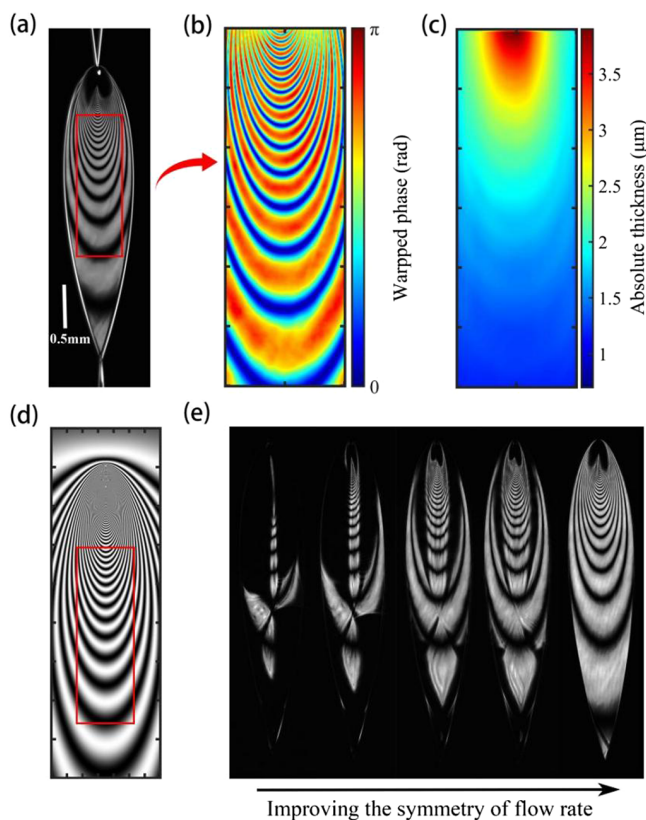
Figure 4. (a) Typical interference fringes of the LST. (b) Wrapped phase in the red box of (a). (c) Thickness distribution unwrapped from (b). (d) Interference fringes corresponding to the thickness distribution of Hasson's model. (e) The change of interference fringes with the improvement of flow symmetry.

flow rate may cause high pressure or atomization of the liquid sheet[19].

Another way to obtain a thinner liquid sheet is to collide the two jets with a misalignment[20,21], as shown in the diagram in Figure 4(c). Our measurements indicate that a larger misalignment leads to a larger deflection angle Δ and a thinner liquid sheet. We prepared an ultra-thin liquid sheet at $\Delta = 60°$, using a mass ratio of 2:3:4 for water, ethanol and glycerol. Figure 4(d) shows the reflectivity spectrum of this ultra-thin liquid sheet, which is in good agreement with the 238 nm theoretical fitting. To our knowledge, this represents the thinnest liquid sheet ever formed by two colliding jets.

4. Flatness measurement

Reflectance spectroscopy measures the thickness at a specific point, and overall knowledge of the thickness distribution and flatness of an LST is also important. It helps us monitor the quality of the as-produced LST and choose the optimal shooting position. In our diagnostic system, an expanded monochromatic continuous wave (CW) laser with

a wavelength of 632.8 nm (indicated by the thick green path in Figure 1(c)) obliquely illuminates the liquid sheet. A charge-coupled device (CCD) is set in the reflection direction to image the interference fringes of the sheet, which can be used to obtain the contour information of the LST's thickness[22–27].

Figure 4(a) shows a typical pattern of interference fringes. In previous works[22–24], the local 1D thickness variation is analyzed according to the interference fringes, but the 2D thickness distribution has not yet been obtained. The sine value of the phase can be potentially derived from the interference fringes, but extracting the thickness distribution is not feasible due to blurriness in the phase. Nonetheless, reconstruction of the thickness distribution for liquid sheets is achievable, as confirmed by our analysis. Here we present the first recovered 2D thickness distribution of the liquid sheet.

Assuming uniform intensity distribution of the expanded beam on the small sheet, the brightness of the interference fringes solely depends on LST reflectivity. The wrapped phase is a single-valued function of thickness at given wavelength and incident angle; hence, we can obtain unique $\sin \delta$ according to Equation (1). The phase obtained is wrapped within a range from 0 to π, as depicted in Figure 4(b). As demonstrated in Figures 3(c) and 3(d), the thickness of the liquid sheet along the z-axis decreases continuously from top to bottom. This implies that the thickness at every interference fringe is $\lambda/2n$ greater than that at the adjacent lower fringe. Based on the prior information, δ can be unwrapped using some classic algorithms[28,29]. Figure 4(c) depicts the retrieved 2D thickness distribution of the LST, where the absolute thickness value was measured through the reflectance spectroscopy measurement at a single point.

It can be seen that the thickness changes significantly in the upper part compared to the relatively flat lower part, where the variation is less than 1 nm within a few micrometers. The spot size of the drive laser in laser-ion acceleration is typically a few micrometers, which means that the change in thickness of the LST within the laser spot is less than 1%. This property makes the lower part more suitable for laser-ion acceleration, as it provides a flat surface with a very small thickness. Research has shown that thin films with a thick middle and thin sides may be more suitable for ultra-intense laser-ion acceleration[30], while LSTs have similar properties and can be selected at locations with different thickness gradients as required.

Interference fringes are not visible near the collision point in Figure 4(a), and we used Hasson's model[31] to calculate the interference fringes, as shown in Figure 4(d). The thickness distribution given by Hasson's model is as follows:

$$h = \frac{R^2 \sin^3\theta}{r(1 - \cos\phi\cos\theta)^2}. \qquad (2)$$

From Equation (2) and Figure 4(d), it can be seen that the theoretical interference fringes closely match the measured fringes, and that the thickness variations are significantly drastic in the vicinity of the collision point. In Figure 4(d), due to the numerical resolution, there are two blurred shadows corresponding to the invisible area in Figure 4(a), as these fringes have to be captured at a very precise angle. Based on the numerical aperture and working distance of the lens in our system, if the angle of the reflected light from the LST deviates by 24.6 mrad, it cannot be detected. If the gradient of thickness variation exceeds 50 nm per micrometer and causes the sheet surface to tilt beyond the collection angle, the fringes cannot be captured.

This phenomenon does not only occur close to the collision point; when the sheet surface bends and no longer behaves like a mirror, the integrity of the interference fringes will be damaged. The unevenness of the LST can be caused by a number of factors, and Figure 4(e) shows a case caused by asymmetry in the flow rate. The sheet is bent and ripples appear on the surface, with the thickness gradient reaching hundreds of nm per micrometer at some positions. The asymmetry of the leftmost subgraph reaches 3% and gradually improves towards the right-hand side until it is completely symmetrical. The asymmetry of the flow rate has such a significant impact on the flatness of the LST that we use two pumps to control the two jets independently, avoiding asymmetry and instability caused by three-way splitting. In fact, we find that different asymmetric factors can cause different bending modes of the liquid sheet, including nonuniformity of mixed solutions, asymmetry of flow rate, unsmooth end face of the capillary, and so on, which are reflected in the interference fringes. This feature allows real-time monitoring of the flatness of the LST, as the sheet is in a constantly changing state, which significantly contributes to the stability and controllability of the liquid sheet.

5. Tilt angle measurement

In laser-ion acceleration, ions generated by the target normal sheath acceleration (TNSA) mechanism are typically emitted perpendicular to the surface of the film[32], which may be the primary mechanism for LSTs[10]. If the target normal is not precisely oriented towards the collimation entrance of the detectors, the measured energy spectra may not be accurate. Furthermore, in applications where ions are collected and transported with magnets[33], the correct orientation of the targets is critical for the designed beam transportation. Our diagnostic system includes a module to measure the tilt angles of LSTs. The method of adjusting the tilt angle of suspended self-supporting LSTs is also provided to ensure correct orientation.

As depicted in Figure 5(a), a reference mirror first replaces the LST and reflects the probe light to CCD2 via a polarization beam splitter (PBS) cube. The image spot on CCD2 serves as the reference position. The reference mirror is then switched to the LST. The change in the position of the spot can be used to calculate the change in the tilt angle based on the object–image relationship. In our system, the probe light is initially rotated to s-polarized by a half-wave plate. After passing through the PBS, the light reflected from the rear surface of the PBS will not enter CCD2. The light reflected from the LST is converted to p-polarized after passing through a quarter-wave plate twice, and will eventually enter CCD2. This compact design effectively eliminates the reflection from the PBS, resulting in a good signal-to-noise ratio for the measurement. The rightmost subgraph in Figure 5(d) shows a typical reflection spot collected by CCD2. The tilt angle of the LST can be calculated from the offset of the center of the reflection spot with respect to the reference position.

Figure 5(b) shows an example measurement of the tilt angle deviation of the LST in 1 hour; the tilt angle of the LST naturally varies by several milliradians. Note that the frequency of the tilt angle measurement depends mainly on the frame rate of the camera, which can reach 10 Hz (see Section 6), and the time interval is not the shortest measurement interval in Figure 5(b). The reason for the long time interval is that the short time jitter of the tilt angle is negligible compared to the long time drift. The reason why we provide a long time interval is that the short-term jitter of the tilt angle is negligible compared to the long-term drift. If the tilt angle deviates significantly for any reason, this diagnosis allows us to detect and recover it in time. The liquid sheet can be precisely controlled to point in the expected direction in two dimensions by adjusting the flow rate of the two pumps and the misalignment of the collision: the former rotates the LST around the x-axis, while the latter rotates around the z-axis.

CCD3 behind the LST is used to image the sheet and the light spot on the sheet (the same CCD in Figure 2(a)). This helps to identify the exact position where the tilt angle of the LST is measured, as the sheet may have different tilt angles at different positions due to distortion. CCD3 and CCD1 also form a spectroscopic path for measuring the thickness of LSTs thinner than 300 nm. Two co-propagating lasers with different wavelengths (632.8 and 1064 nm, respectively) are irradiated onto CCD1 and CCD3, as shown in Figure 5(c), and then the reflectivity of the film is calculated by measuring the integrated light intensity of CCD1 and CCD3 simultaneously to eliminate the impact of light source jitter. A pure and smooth film such as a liquid sheet can exhibit minimal surface scattering, and thus its absolute reflectance is measured. The theoretical reflectivity, calculated from Equation (1), is illustrated by the two sine curves in Figure 5(c), while the red pentagram denotes the reflectivity
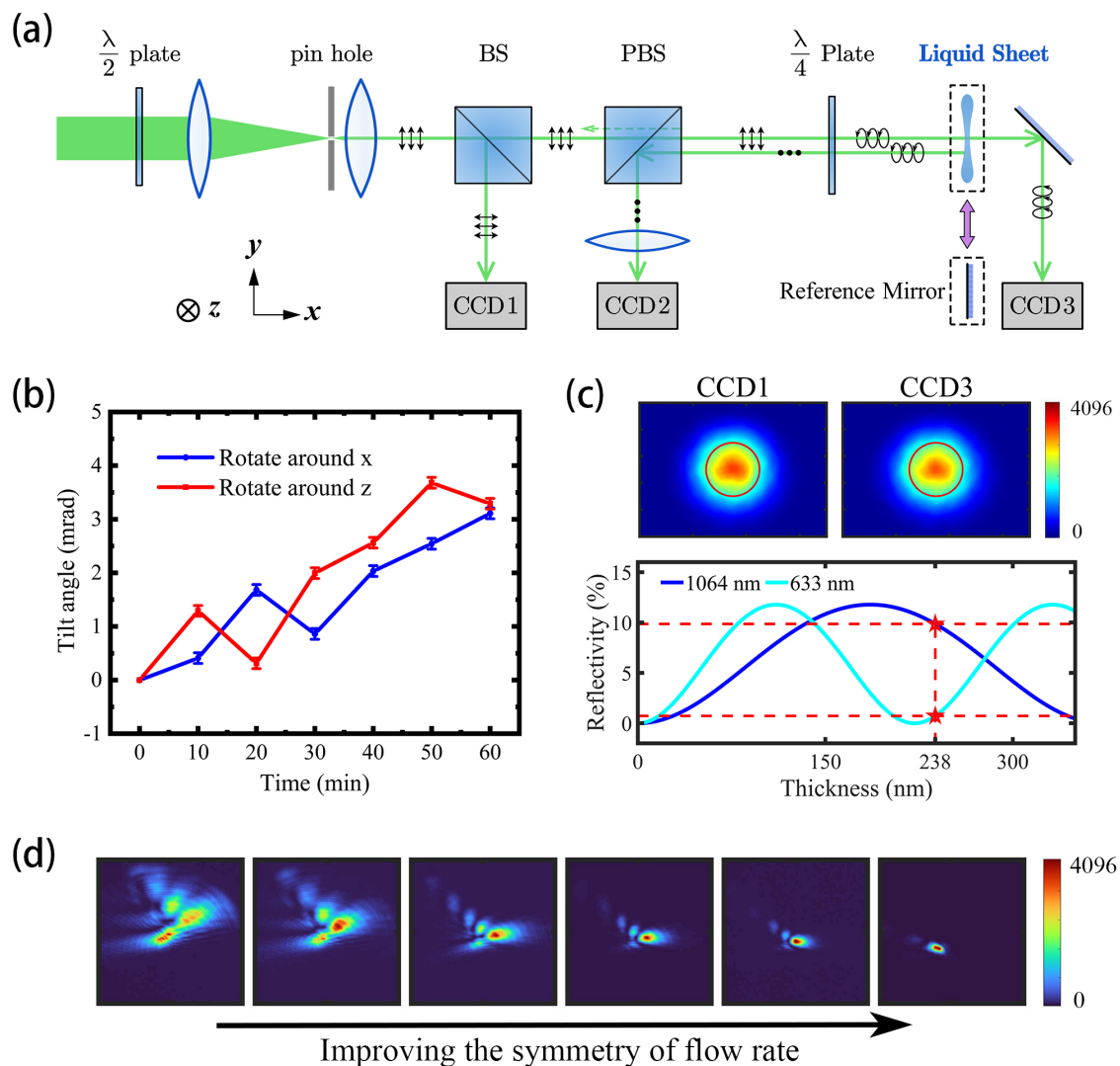
Figure 5. (a) Schematic diagram of the tilt angle measurement. (b) The tilt angle change within 1 hour. (c) The intensity integral of CCD1 and CCD3 to calculate the absolute reflectivity of the LST. (d) The change of the spot collected by CCD2 with the improvement of flow symmetry.

measured at two distinct wavelengths. Analysis of these data suggests a film thickness of 238 nm, which is consistent with the results presented in Section 3 at 238 nm.

Furthermore, CCD2 not only diagnoses the tilt angle of the sheet, but also provides more information about the flatness of the sheet near the measurement point. The distortion of the sheet caused by the imbalance of the two colliding jets would result in an aberrant image of the spot, similar to that caused by a non-flat mirror. By adjusting the jets, an ideal reflection spot can be achieved, as illustrated in Figure 5(d). As the symmetry of the flow rate improves, the center of the reflected spot gradually shifts, indicating that the tilt angle of the LST is changing. Compared to Figure 4(e) with 3% flow asymmetry, the method in Figure 5(d) provides a more accurate but more localized characterization of flatness with only 1% flow rate asymmetry.

6. Discussion

Accuracy of measurement is one of the most important parameters of the diagnostic system. Two methods were used to measure the thickness of the 238 nm liquid sheet: the reflectance spectroscopy described in Section 3, and the reflectivity method described in Section 5 (see Figure 5(c)). The reflectance spectroscopy method has been calibrated with the commercial product used in the literature[9], and shown good agreement with it. The accuracy of this method depends mainly on the accurate matching of the measured spectrum, that is, the value of h that minimizes the following expression:

$$\min\left\{\int_{\lambda_1}^{\lambda_2}[I(\lambda)-R(h,\lambda)]^2\mathrm{d}\lambda\right\}, \tag{3}$$

Table 1. Parameters of each measurement module.

Module number	A	B	C	D
Measured metric	Thickness	Flatness	Tilt angle	Position
Frequency	~10 Hz	~10 Hz	~10 Hz	~1 kHz
Range	0.01–50 μm	0–50 nm/μm	0–25 mrad	0–1 mm
Accuracy	±0.5% (>200 nm) ±2 nm (<300 nm)	±0.1 nm/μm	±0.2 mrad	±2 nm
Spatial resolution	~20 μm	~5 μm	~20 μm	~20 μm
Conflict	/	/	D	C
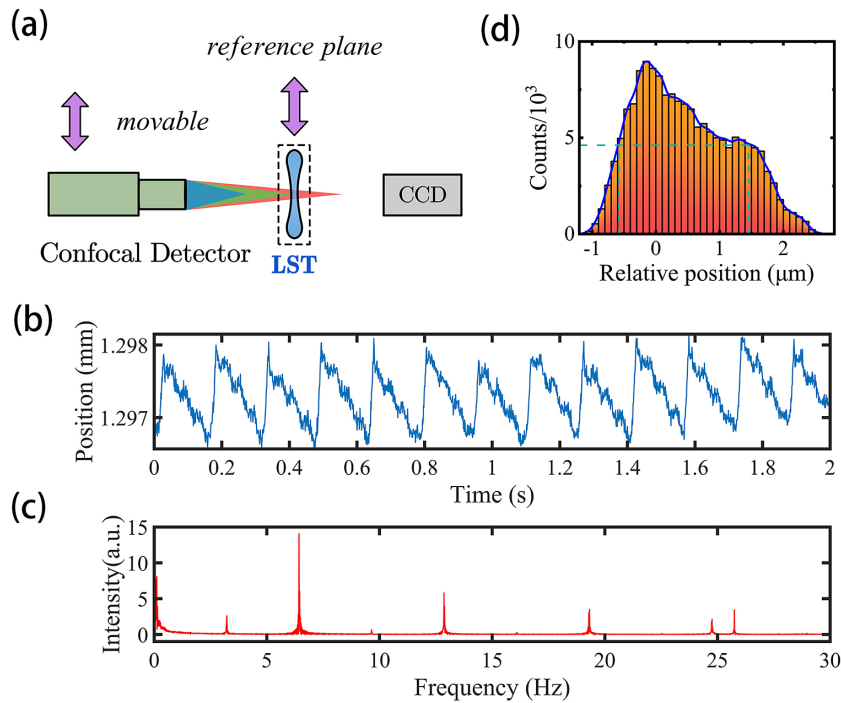
Figure A1. (a) Schematic diagram of position measurement. (b) Time domain of the LST's position (distance to the confocal detector). (c) Frequency domain of the LST's vibration in (b). (d) Histogram of the LST's relative position within 10 minutes.

where $I(\lambda)$ is the measured reflectivity spectrum, $R(h,\lambda)$ is the theoretical reflectivity and λ_1 and λ_2 are the upper and lower limits of the wavelength, respectively. The relationship between thickness and wavelength can be expressed as $\frac{\Delta h}{h} = \frac{\Delta \lambda}{\lambda} - \frac{\Delta n}{n}$. In our system, the measurement accuracy can reach $\frac{\Delta h}{h} < 0.5\%$, which is ±0.5%. The error of the ultra-thin film measurement is 238 ± 1.2 nm.

The resolution of the reflectivity method for s-polarized light can be represented by the following equation:

$$\left(\frac{\partial R}{\partial h}\right)^{-1} \tag{4}$$
$$= \frac{\lambda \left\{4\cos^2\theta \left[n^2(\lambda) - \sin^2\theta\right] + \left[n^2(\lambda) - 1\right]^2 \sin^2\left[2\pi h\sqrt{n^2(\lambda) - \sin^2\theta}/\lambda\right]\right\}^2}{8\pi \cos^2\theta \left[n^2(\lambda) - \sin^2\theta\right]^{\frac{3}{2}} \left[n^2(\lambda) - 1\right]^2 \sin\left[4\pi h\sqrt{n^2(\lambda) - \sin^2\theta}/\lambda\right]}.$$

Assuming that $n = 1.43$, $\theta = 0°$, $\lambda = 633$ nm, when the measured thickness is 238 nm, the result calculated from Equation (4) is $\Delta h/\Delta R \approx 1175$ nm. If $\Delta R < 0.1\%$ (this has

been validated), then $\Delta h < 1.175$ nm. This means that the thickness measurement result with error is 238 ± 1.2 nm. This is consistent with that measured by reflectance spectroscopy. In most cases, the error measured by this method is within ±2 nm.

The accuracy of the tilt angle measurement is determined by the object–image relationship and the physical resolution of the CCD. The reflected spot can be detected by moving at most 5 pixels, and the field angle for the liquid sheet in our system is 0.2 mrad, which is sufficient for tilt angle diagnosis in laser-ion acceleration. The resolution can be adjusted by the user setting the object–image relationship.

The characteristics of each module are summarized in Table 1, and an introduction to position measurement is given in the Appendix.

In summary, we have developed a device for online measurement of the LST thickness, and realized the reconstruction of thickness distribution of the LST from the interference fringes for the first time. An ultra-thin 238 nm

liquid sheet was produced by using the appropriate ternary liquid phase solution and misalignment of jets. The proposed methods and liquid sheet control are valuable for laser-ion acceleration as well as other applications[27,34–38]. The system is also well-suited for the high-precision, real-time diagnosis of other transparent targets, such as plastic films or liquid crystal films[39].

Appendix: Position measurement

The results of laser-ion acceleration are closely related to the relative positions of the laser focal spot and the target. Unlike solid films whose positions can be identified by defects or pollutants[40], a liquid sheet is transparent and flawless, and thereby we utilized a confocal displacement detector (Micro-Epsilon, confocalDT 2421) to measure the position of the LST.

The detector is arranged in the normal direction of the LST and can be moved by a linear stage, as shown in Figure A1(a). We first used a reference object to define this plane, and then used a CCD with a very small depth of field (a few μm) to image it clearly. The drive laser was also focused on this plane. The confocal detector is then used to measure the position of the LST and align it with the focusing plane.

Figure A1(b) shows the periodic vibration of the LST position. We analyzed it in the frequency domain, as shown in Figure A1(c), revealing that the vibration can be attributed to specific frequencies. The 6 Hz vibration and its multiples are derived from the pump plunger motion, while the rest include capillary vibration, platform inherent vibration, and so on. Figure A1(d) is a histogram of the position (or vibration amplitude) of an LST within 10 minutes after optimization. Its full width at half maximum (FWHM) is about 2 μm, which is smaller than the Rayleigh length of the focused laser. Relevant discussions on suppressing the jitter can be found in our previous publication[14].

References

1. A. Higginson, R. Gray, M. King, R. Dance, S. Williamson, N. Butler, R. Wilson, R. Capdessus, C. Armstrong, and J. Green, Nat. Commun. **9**, 724 (2018).
2. P. Wang, Z. Gong, S. G. Lee, Y. Shou, Y. Geng, C. Jeon, I. J. Kim, H. W. Lee, J. W. Yoon, and J. H. Sung, Phys. Rev. X **11**, 021049 (2021).
3. H. Daido, M. Nishiuchi, and A. S. Pirozhkov, Rep. Prog. Phys. **75**, 056401 (2012).
4. M.-C. Vozenin, J. Bourhis, and M. Durante, Nat. Rev. Clin. Oncol. **19**, 791 (2022).
5. W. Ma, V. K. Liechtenstein, J. Szerypo, D. Jung, P. Hilz, B. Hegelich, H. Maier, J. Schreiber, and D. Habs, Nucl. Instrum. Methods Phys. Res. A **655**, 53 (2011).
6. W. Ma, I. J. Kim, J. Yu, I. W. Choi, P. Singh, H. W. Lee, J. H. Sung, S. K. Lee, C. Lin, and Q. Liao, Phys. Rev. Lett. **122**, 014803 (2019).
7. Y. Shou, P. Wang, S. G. Lee, Y. J. Rhee, H. W. Lee, J. W. Yoon, J. H. Sung, S. K. Lee, Z. Pan, and D. Kong, Nat. Photonics **17**, 137 (2023).
8. M. Ehret, J. I. Apiñaniz, J. L. Henares, R. Lera, D. de Luis, J. A. Pérez-Hernández, L. Volpe, and G. Gatti, Nucl. Instrum. Methods Phys. Res. B **541**, 165 (2023).
9. K. George, J. Morrison, S. Feister, G. Ngirmang, J. Smith, A. Klim, J. Snyder, D. Austin, W. Erbsen, and K. Frische, High Power Laser Sci. Eng. **7**, e50 (2019).
10. J. T. Morrison, S. Feister, K. D. Frische, D. R. Austin, G. K. Ngirmang, N. R. Murphy, C. Orban, E. A. Chowdhury, and W. Roquemore, New J. Phys. **20**, 022001 (2018).
11. P. Puyuelo-Valdes, D. de Luis, J. Hernandez, J. Apiñaniz, A. Curcio, J. Henares, M. Huault, J. Pérez-Hernández, L. Roso, and G. Gatti, Plasma Phys. Control Fusion **64**, 054003 (2022).
12. M. Rehwald, S. Assenbaum, C. Bernert, F.-E. Brack, M. Bussmann, T. E. Cowan, C. B. Curry, F. Fiuza, M. Garten, and L. Gaus, Nat. Commun. **14**, 4009 (2023).
13. F. Treffert, C. Curry, H.-G. Chou, C. Crissman, D. DePonte, F. Fiuza, G. Glenn, R. Hollinger, R. Nedbailo, and J. Park, Appl. Phys. Lett. **121**, 074104 (2022).
14. Z. Cao, Z. Peng, Y. Shou, J. Zhao, S. Chen, Y. Gao, J. Liu, P. Wang, Z. Mei, and Z. Pan, Front. Phys. **11**, 231 (2023).
15. W. Ma, Z. Liu, P. Wang, J. Zhao, and X. Yan, Acta Phys. Sin. **70**, 084102 (2021).
16. R. Li and N. Ashgriz, Phys. Fluids **18**, 087104 (2006).
17. M. Born and E. Wolf, *Principles of Optics: Electromagnetic Theory of Propagation, Interference and Diffraction of Light* (Elsevier, Amsterdam, 2013).
18. A. Watanabe, H. Saito, Y. Ishida, M. Nakamoto, and T. Yajima, Opt. Commun. **71**, 301 (1989).
19. J. W. Bush and A. E. Hasha, J. Fluid Mech. **511**, 285 (2004).
20. M. Panao and J. Delgado, Phys. Fluids **25**, 012105 (2013).
21. S. Kashanj and A. Kebriaee, Chem. Eng. Sci. **206**, 235 (2019).
22. G. Galinis, J. Strucka, J. C. Barnard, A. Braun, R. A. Smith, and J. P. Marangos, Rev. Sci. Instrum. **88**, 083117 (2017).
23. J. D. Koralek, J. B. Kim, P. Brůža, C. B. Curry, Z. Chen, H. A. Bechtel, A. A. Cordones, P. Sperling, S. Toleikis, and J. F. Kern, Nat. Commun. **9**, 1353 (2018).
24. S. Menzi, G. Knopp, A. Al Haddad, S. Augustin, C. Borca, D. Gashi, T. Huthwelker, D. James, J. Jin, and G. Pamfilidis, Rev. Sci. Instrum. **91**, 105109 (2020).
25. D. J. Hoffman, T. B. Van Driel, T. Kroll, C. J. Crissman, E. S. Ryland, K. J. Nelson, A. A. Cordones, J. D. Koralek, and D. P. DePonte, Front. Mol. Biosci. **9**, 1048932 (2022).
26. C. J. Crissman, M. Mo, Z. Chen, J. Yang, D. A. Huyke, S. H. Glenzer, K. Ledbetter, J. P. F. Nunes, M. L. Ng, and H. Wang, Lab Chip. **22**, 1365 (2022).
27. J. C. Barnard, J. P. Lee, O. Alexander, S. Jarosch, D. Garratt, R. Picciuto, K. Kowalczyk, C. Ferchaud, A. Gregory, and M. Matthews, Front. Mol. Biosci. **9**, 1044610 (2022).
28. R. M. Goldstein, H. A. Zebker, and C. L. Werner, Radio Sci. **23**, 713 (1988).
29. H. S. Abdul-Rahman, M. A. Gdeisat, D. R. Burton, M. J. Lalor, F. Lilley, and C. J. Moore, Appl. Opt. **46**, 6623 (2007).
30. M. Chen, A. Pukhov, T. Yu, and Z. Sheng, Phys. Rev. Lett. **103**, 024801 (2009).
31. D. Hasson and R. E. Peck, AIChE J. **10**, 752 (1964).
32. R. Snavely, M. Key, S. Hatchett, T. Cowan, M. Roth, T. Phillips, M. Stoyer, E. Henry, T. Sangster, and M. Singh, Phys. Rev. Let. **85**, 2945 (2000).
33. J. Zhu, M. Wu, Q. Liao, Y. Geng, K. Zhu, C. Li, X. Xu, D. Li, Y. Shou, and T. Yang, Phys. Rev. Accel. Beams **22**, 061302 (2019).
34. Z.-H. Loh, G. Doumy, C. Arnold, L. Kjellsson, S. Southworth, A. Al Haddad, Y. Kumagai, M.-F. Tu, P. Ho, and A. March, Science **367**, 179 (2020).

35. J. Yang, R. Dettori, J. P. F. Nunes, N. H. List, E. Biasin, M. Centurion, Z. Chen, A. A. Cordones, D. P. Deponte, and T. F. Heinz, Nature **596**, 531 (2021).
36. M.-F. Lin, N. Singh, S. Liang, M. Mo, J. Nunes, K. Ledbetter, J. Yang, M. Kozina, S. Weathersby, and X. Shen, Science **374**, 92 (2021).
37. Y. E, L. Zhang, A. Tsypkin, S. Kozlov, C. Zhang, and X.-C. Zhang, J. Opt. Soc. Am. B **39**, A43 (2022).
38. C.-L. Xia, Z.-L. Li, J.-Q. Liu, A.-W. Zeng, L.-J. Lü, and X.-B. Bian, Phys. Rev. A **105**, 013115 (2022).
39. P. Poole, C. Andereck, D. Schumacher, R. Daskalova, S. Feister, K. George, C. Willis, K. Akli, and E. Chowdhury, Phys. Plasmas **21**, 063109 (2014).
40. Y. Shou, D. Wang, P. Wang, J. Liu, Z. Cao, Z. Mei, Y. Geng, J. Zhu, Q. Liao, and Y. Zhao, Nucl. Instrum. Methods Phys. Res. A **927**, 236 (2019).